Exploring hybrid imogolite nanotubes formation via Si/Al stoichiometry control

Pierre Picot, Yuan Yuan Liao, Elodie Barruet, Frédéric Gobeaux, Thibaud Coradin, Antoine Thill

Exploring hybrid imogolite nanotubes formation via Si/Al stoichiometry control

Pierre Picot,[1] Yuanyuan Liao,[1] Elodie Barruet,[1] Frédéric Gobeaux,[1] Thibaud Coradin,[2] Antoine Thill.[1*]

[1] LIONS, NIMBE, CEA, CNRS, Université Paris-Saclay, CEA-Saclay, 91191, Gif-sur-Yvette, France.

[2] Sorbonne Universités, UPMC Univ. Paris 06, CNRS, Collège de France, Laboratoire de Chimie de la Matière Condensée de Paris (LCMCP), 4 place Jussieu, 75005, Paris, France.

* Corresponding author: Antoine Thill; antoine.thill@cea.fr

Abstract

Hybrid imogolite aluminosilicate nanotubes with methylated internal surface can be obtained by introduction of the corresponding organosilane during their synthesis. However, similarly to pristine imogolite, a number of side-products, including proto-imogolite (open-imoLS), allophanes and aluminum hydroxides, are formed, that ultimately impact on the properties of the dispersions. In order to minimize the proportion of these side-products, we have here systematically explored the impact of the initial Si/Al ratio on the content of hybrid imogolite dispersions before and after dialysis. By combining cryo-TEM, ICPMS, IR spectroscopy and Small Angle X-ray Scattering, we evidenced that the Si/Al ratio has a large impact on the formation of aluminum hydroxides that can be minimized with a slight excess of Si precursor. However, a large excess of Si is detrimental to the reaction yield leading to an important proportion of proto-imogolite. We propose that the optimal Si/Al ratio of *ca*. 0.6 can both minimize the proportion of aluminum hydroxides and proto-imogolite. These results suggest that the dynamic and therefore reactive character of Imogolite dispersions may have been so far underlooked.

Introduction

Controlling the polymorphism of aluminosilicate compounds is critical point in order to understand their properties and for their potential applications as catalyst or water remediation compounds.[1-3] At this scale, the properties of materials are mainly controlled by the surface, and so the shape, the size and the groups present. For instance, polymorph minerals (sillimanite, andalusite and kyanite) with the same chemical formula (Al_2SiO_5) and different crystal structures (tetrahedral, trigonal bipyramidal and octahedral) do not have the same behavior with collector molecules.[4] Even if nucleation and growth processes of these materials are still not well understood, the modification of the synthesis parameter allows to control the crystal polymorphism.[5, 6]

Imogolite is a natural aluminosilicate nanotube discovered in 1962 by Aomine and Yoshinaga in volcanic soils.[7] Since then, it has attracted large attention due to its uncommon structure within the

aluminosilicate clay family.[8-17] Compared to other 1:1 TO or 2:1 TOT aluminosilicate clay minerals, imogolite displays an unusual Si/Al molar ratio of 0.5 and a very special chemical environment for the Si. Silicon atoms do not form a polymerized tetrahedral layer exposing siloxane groups at the surface. Instead, each silicon atom is bonded by three Si–O–Al bonds on top of the lacuna of an aluminum dioctahedral layer exposing silanol groups at the surface. The Imogolite Local Structure (ImoLS) can then be refereed as 0.5:1 TO. Several different nanostructures (Allophane, proto-imogolite, Imogolite) which can be considered as imoLS polymorphs share the ImoLS. All these shapes have in common a very high curvature.

A large size mismatch exists between the edge size of relaxed Si tetrahedra and the O–O distance in a flat aluminum dioctahedral layer. The ImoLS relaxes this size mismatch by adopting a very important curvature with the Si tetrahedra confined inside a tubular or spherical structure. This is probably not the only factor explaining the curvature. The internal Si–OH groups are believed to form intramolecular hydrogen bonds, which favor a zig-zag configuration of the nanotubes.[18] With an external diameter of about 2 nm for natural imogolite nanotubes, this clay mineral is, to our knowledge, the single-walled inorganic nanotube with the highest curvature.

In the late 70s, Farmer et al. proposed a synthetic route to imogolite consisting in mixing a silicon precursor (mentioned as SiO_2 monomers in this publication) and an aluminum ($AlCl_3$) precursor with a precise control of pH.[19] The resulting synthetic imogolite nanotubes exhibit a slightly larger diameter than the natural ones (2.4 nm) mainly because of the temperature of formation.[20] They have a length between few tens of nanometer to few microns and an average chemical composition of $(HO)_3Al_2O_3Si(OH)$. These nanotubes are easily dispersed in water and have different chemical groups on their internal (Si-OH) and external (Al-OH-Al) surfaces that can be independently modified or functionalized.[21-29] For instance, by changing the usual silicon precursor tetraethoxysilane for a triethoxymethylsilane (TEMS) it is possible to synthesize methyl-imogolite (imo-CH_3).[30] These hybrid nanotubes have a larger diameter, probably due to the loss of intramolecular hydrogen bonds network, and an internal cavity entirely covered with methyl groups. The external surface is chemically unchanged and hydrophilic. However, the imo–CH_3 have a lower positive charge than the pristine synthetic imogolite in water,[31] forming stable dispersion of small bundles of nanotubes.[32] DFT calculations also show that methylation of the internal cavity result in a reduced value of the surface dipole density from about 22 $pC{\cdot}m^{-1}$ for classical imogolite to 14 $pC{\cdot}m^{-1}$ for imo-CH_3.[33] This new material can be seen as an inorganic 1D micelle as it provides a hydrophobic 1D nanochannel dispersed in water. Therefore, it has many promising properties such as (i) the trapping of small organic molecules,[34] (ii) the extraction of hydrophobic dyes,[35] (iii) the confinement of water[36] and (iv) gas separation ability.[30]

As for the pristine imogolite, the early stages of methyl-imogolite synthesis involve the formation of proto-imogolite, which has the local structure of imogolite.[37] These initial species, recently called open-ImoLS, then evolve by curving and finally closing into imogolite or allophane (the spherical analogue of imogolite, also called spherical closed-ImoLS) depending on the experimental conditions.[38] It has been shown that the amount of open-ImoLS decreases as the nanotubes form but significant concentration can persist even after prolonged synthesis time.[39] It is also possible that a fraction of allophane formed at the early stage of the synthesis remains in the dispersion.[38] Other phases that can form along with imoLS polymorphs are aluminum hydroxides. These minerals occur as micron-sized crystals that scatter light very efficiently leading to turbid dispersions. Boyer et *al.* showed that changing the acid, HCl instead of $HClO_4$, or the silicon precursor, trimethoxymethylsilane (TMMS) instead of TEMS, leads to a decrease of the dispersion turbidity and an increase in the average length of the nanotubes.[32] Zanzottera reported that a slight excess of TEMS (when compared to the imogolite stoichiometry of two aluminum per silicon) allows for preventing the formation of gibbsite (γ-$Al(OH)_3$).[40] Only very few quantitative studies have been performed on the evolution of the weight fraction of the proto-imogolite during the synthesis.[34, 39]

Consequently, the quantification and the determination of conditions minimizing side products are major points in order to properly characterize the nanotubes. This is particularly essential for properties (adsorption capacity, surface charge, film formation…) which greatly depend on the morphology (sheets, tiles, spheres, tubes, bundles) or the surface (groups, hydrophobic or hydrophilic…).

As a step further towards the understanding and control of hybrid imogolite formation, we have here investigated in a systematic manner the impact of the initial Si/Al molar ratio on the composition of imo-CH_3 dispersion. Cryo-TEM examination evidenced an evolution from aluminum hydroxide-rich to open-ImoLS-rich suspension that was confirmed by ICPMS and IR spectroscopy. From these data, an optimal ratio Si/Al that minimizes both side-products could be identified. Further structural investigations using SAXS in the two different regimes allowed us to provide an explanation for the existence of this critical ratio that originates from the specific structure and reactivity of open-ImoLS.

Methods

Synthesis of methyl-imogolite

Imo–CH_3 was prepared using a protocol inspired by Bottero et *al*.[30] Briefly, aluminum-tri-sec-butoxide (ASB) was added to one liter of a HCl_{aq} solution (20 mM) with a HCl/Al molar ratio of 0.5 and stirred during one hour. Then, the sample was split in nine solutions of 100 mL. Trimethoxymethylsilane (TMMS) was added to obtain an increasing Si/Al molar ratio from 0.5 for the first solution (sample 1) up to 0.7 for the last one (sample 9), *i.e*. with a 0.025 increment between two successive solutions. The dispersions were kept in an oven for 7 days at 90°C. After heating, the dispersions were dialyzed against MilliQ water using a 10 kDa membrane until the conductivity of the external phase reaches 2 $\mu S \cdot cm^{-1}$.

Cryo-TEM

Cryo-TEM was performed using a JEOL 2010 FEG microscope operated at 200 kV at low temperature (-180°C). The defocus was set between 0 and 7000 nm depending on the magnification. Images were recorded with a Gatan camera. Drops of the dispersions were deposited on EM grids covered with a holey carbon film (Quantifoil R2/2) previously treated with a plasma glow discharge. The excess liquid on the grids was blotted out with filter paper, and the grids were quickly immersed in liquid ethane to form a thin vitreous ice film. The whole process was conducted using a Vitrobot apparatus (FEI Company).

Inductively Coupled Plasma Mass Spectrometry

ICPMS measurements were performed using a quadrupole ICPMS ICAPQ (ThermoFisher Scientific). The standards used were SPEX CertiPrep Silicon 10 000 ppm and PlasmaCAL Aluminum 1 000 ppm. The calibrations for aluminum and silicon were external. The range of concentrations studied was 25 to 250 ppm for silicon and 50 to 500 ppm for aluminum. All dilutions were prepared using sub boiled distilled HNO_3 at 2% in MilliQ water and weighted. ICAPQ was used in KED mode in order to avoid CO_2 interferences.

Fourier transform infrared spectroscopy

Infrared (IR) spectra were recorded using a Bruker Vertex 70 FTIR spectrometer at RT. About 1 mg of dry sample powder was mixed with 100 mg of KBr powder and pressed into an IR transparent disk. 200 scans between 400 cm^{-1} and 4000 cm^{-1} with a resolution of 4 cm^{-1} were recorded and averaged. All the spectra were treated using OPUS software (OPUS 7.2), subtracted from KBr, corrected from water using OPUS H_2O/CO_2 compensation and the baselines were corrected using OPUS baseline correction.

Small Angle X-Ray scattering

Small angle X-ray scattering (SAXS) is a powerful technique to probe the size, shape, polydispersity and concentration of nanoparticles *in situ*. SAXS data have been collected on the SWING beamline at SOLEIL, the national French synchrotron facility. The q range is set to $3.2 \times 10^{-2} – 1$ $Å^{-1}$, with $q = 4\pi\sin(\theta)/\lambda$, where 2θ is the scattering angle and $\lambda = 0.82655$ Å is the X-ray wavelength. The beam size is 0.4×0.1 mm, and the flux is about 10^{12} photon·s^{-1}. The SAXS measurements were performed using a Kapton capillary with a 1 mm beam path length. The scattering picture was obtained every minute on the detector with an exposure time of 1 s. The images captured by the AVIEX170170 CCD detector were radially averaged and corrected for transmitted intensity using a dedicated application at the beamline. Intensities were subsequently converted to absolute units using the zero angle extrapolated scattered intensity of water as reference. The measurement of an empty cell was used as a reference for intensity subtraction of the Kapton windows.

Results and discussion

Cryo-TEM

After the dialysis step, the first three samples, with the lowest initial Si/Al ratio, are slightly turbid whereas the others display no turbidity (Figure S1). To get an insight into the dispersion composition, the samples with initial Si/Al ratio ranging from 0.5 (sample 1) to 0.7 (sample 9) were imaged after dialysis using cryo-TEM (Figure 1). For all of them, it is possible to see nanotubes with a length of few hundreds of nanometer that can be attributed to imogolite. Moreover, most of these imogolites are associated in bundles of 2 to 4 tubes (Figure S2), coated with spherical shaped compounds, which can also agglomerate between the nanotubes (Figure S3). The diameter of these nanotubes is around 3 nm, similar to the one obtained by X-ray diffraction or SAXS measurements.[30, 32, 34, 35] On the TEM grids, platelets with typical hexagonal shape that can be attributed to aluminum hydroxides of the gibbsite type are occasionally observed with sizes ranging from 100 nm to 500 nm (Figure S4).

From the analysis of at least fifteen images per samples, we conclude that the proportions of the aluminum hydroxide and of the small spherical compounds are roughly correlated to the initial Si/Al ratio. The aluminum hydroxide impurities are frequently observed and have a large size (close to 500 nm) when the initial Si/Al ratio is below 0.6 (samples 1 to 3), whereas both their size and concentration decrease for Si/Al ratio above 0.6 (samples 4 to 9). Regarding spherical particles, they are only present at the surface of tubes for initial ratios below 0.6 whereas clusters of few tens of nanometers between the bundles of imogolite are clearly evidenced above this ratio. Based on the literature, these spherical particles should correspond to open-ImoLS or spherical closed-ImoLS. Thill et *al.* showed that a size threshold exists, which separates a regime of spherical curvature for small open-ImoLS and tubular curvature for large open-ImoLS.[41] Du et *al.* describes a pathway explaining the formation and the coexistence of spherical and tubular compounds in the final dispersion after the heating stage.[38] In this scenario, the proportion of spheres and tubes in the final dispersion would be linked to the distribution in size and shape of the open-ImoLS. Increasing the Si/Al molar ratio also increases the initial proportion of partially or totally hydrolyzed Si tetrahedra available to react with the sheets of aluminum octahedra. These first amorphous compounds already exhibit a curvature that may reduce or suppress the growth of larger sheets of aluminum hydroxides. When the initial Si/Al ratio is above 0.60 cryo-TEM images tend to show that the proportion of spherical closed-ImoLS and sphere clusters increases. The persistence of these clusters of spheres means that the spherical curvature somehow blocks the ImoLS in a spherical shape and their aggregation does not enable a sphere/tube transition.

To sum up, the increase of the initial Si/Al ratio decreases the size and proportion of aluminum hydroxides in the final dispersion. However, if the ratio is higher than 0.6, an increasing proportion of persistent spherical closed/open-ImoLS occurs. Therefore, an optimal ratio close to 0.6 exists for which both the concentration of aluminum hydroxide and of the spherical closed/open-ImoLS is minimized.

This qualitative scenario established through cryo-TEM observations needs to be reinforced by quantitative data. In the following sections, we will examine the ICPMS, IR spectra and SAXS curves of the dispersions in order to try to improve the quantifications of the side products (aluminum hydroxides and spherical closed/open-ImoLS).

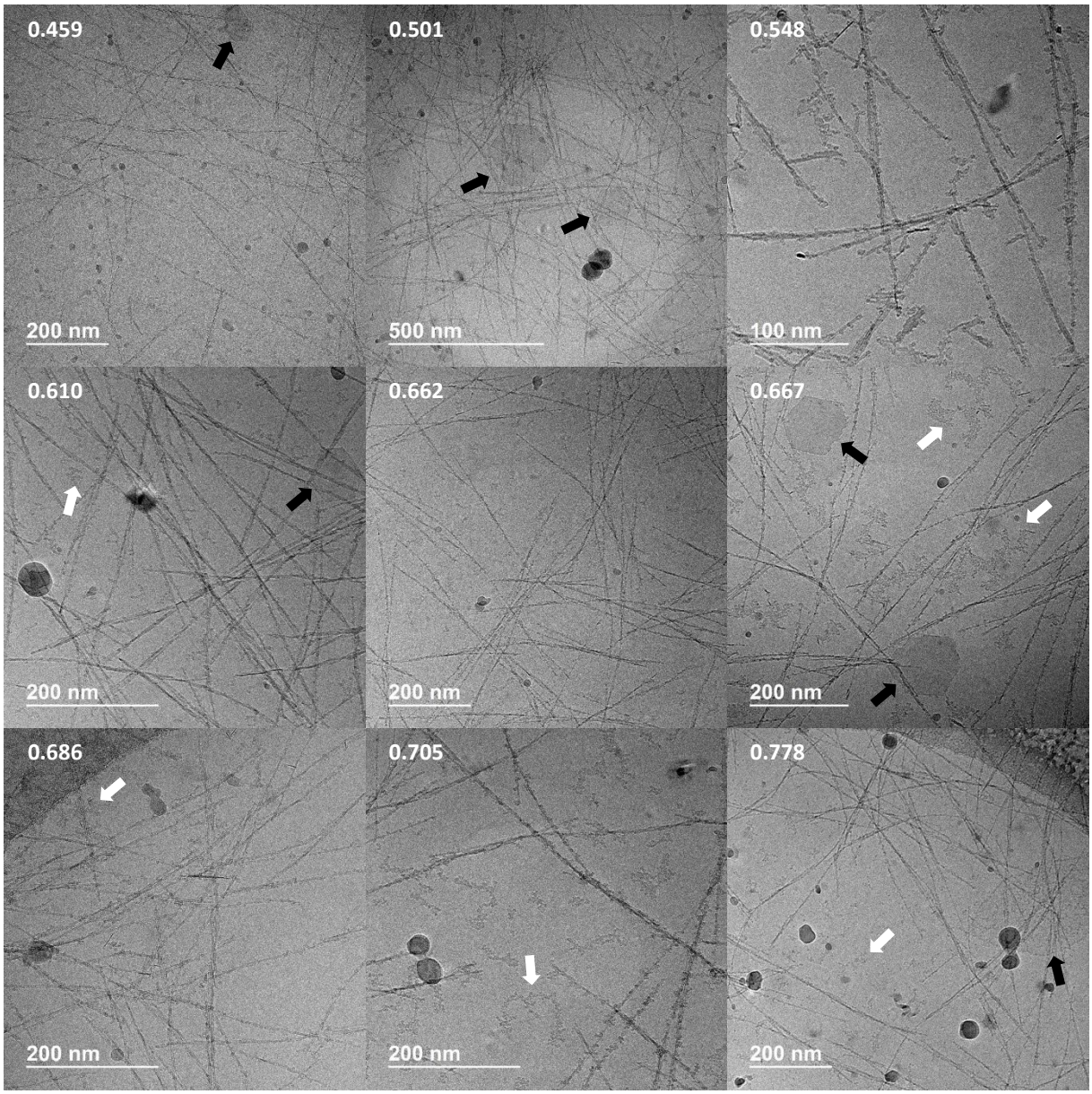

Figure 1 - Cryo-TEM images of the nine samples. Black and white arrows respectively highlight aluminum hydroxides and sphere clusters (closed/open-ImoLS) between the tubes. Si/Al ratio before dialysis are written on their corresponding pictures.

ICPMS

Figure 2 shows the data obtained from ICPMS measurements of aluminum and silicon elements and the resulting Si/Al ratio, before (diamonds) and after (circles) dialysis. For sake of comparison, dashed lines corresponding to theoretical (*i.e*. initial) molar ratio/concentration and dotted lines to imogolite ratio (*i.e*. two aluminum per silicon) were added. As mentioned in the experimental part, one liter of HCl_{aq} with ASB is prepared and split in nine solutions after one hour of mixing. However, when the splitting is performed, the dispersion remains turbid and large particles are still visible. This may explain why the concentrations measured before dialysis do not perfectly match the theoretical ones, especially for Al concentration.

Before dialysis, the molar ratio Si/Al ranges from 0.45 to 0.78. The dialysis induces a decrease of both aluminum and silicon concentrations in the dispersions, with a more significant variation for Si. As a result, the Si/Al ratio is also strongly impacted by the dialysis step. From these data, it is possible to distinguish two regimes. In the first regime, initial molar Si/Al ratios are below 0.65 (samples 1 to 5) then the final (*i.e*. post-dialysis) ratios are smaller than that of imogolite. In the second regime, initial molar ratios are above 0.65 (samples 6 to 9) and the final ratios are close to the expected imogolite ratio of 0.5

In the first regime, the smaller Si/Al ratio in the dispersions can be assigned to the presence of aluminum hydroxides (typically gibbsite) or to some Si lacunae in the imogolite structure. In the second regime, either only stoichiometric imogolite is formed or the presence of aluminum hydroxide in the final dispersions is compensated by the presence of amorphous silica compounds or by Al lacunae in the imogolite structure. Finally, for some samples the Si/Al ratio measured after dialysis is above the stoichiometric one of imogolite. This can be attributed to open-ImoLS species that have the same chemical composition as imogolite if the edges of the particles are neglected. Indeed, if there are some Si tetrahedra linked to Al octahedral on these edges through Si–O–Al bounds, the Si/Al ratio for open-ImoLS can be above 0.5 (Figure S5). Scheme 1 illustrates this effect using model open-ImoLS constructed as already described where border silicon atoms are added.[41]

Using ICPMS measurements, it is possible to quantify the proportions of aluminum hydroxide or lacuna in the final dispersions. The molar ratio R between silicon and aluminum is defined by:

$$R = \frac{Si_{total}}{Al_{total}} \tag{1}$$

For silicon, the origins are: amorphous silica, closed/open-ImoLS and imogolite. For aluminum, the origins are: aluminum hydroxides, closed/open-ImoLS and imogolite. Equation (1) can be written:

$$R = \frac{Si_{silica} + Si_{ImoLS} + Si_{imogolite}}{Al_{hydroxides} + Al_{ImoLS} + Al_{imogolite}} \tag{2}$$

If the excess is only due to aluminum hydroxide and assuming that the dialysis eliminates amorphous silica but does not induce silicon deficiencies in imogolite or closed/open-ImoLS then equation (2) can be simplified:

$$R = \frac{Si_{imogolite}}{Al_{hydroxides} + Al_{imogolite}} \tag{3}$$

Leading to:

$$\frac{Al_{hydroxides}}{Al_{imogolite}} = 0.5 * \left(\frac{1}{R} - 2\right) \quad (4)$$

Then:

$$x^{Al}_{imogolite} = 2 * R \quad (5)$$

With:

$$x^{Al}_{imogolite} = \frac{Al_{imogolite}}{Al_{tot}} = 1 - x^{Al}_{hydroxides}$$

Applying equation (5) to the case of sample 1 with a measured ratio of 0.343 (after dialysis), the proportion of aluminum in imogolite is 68.6%. Assuming that aluminum hydroxides mostly consist in gibbsite impurities, the weight proportion of gibbsite would be 26.7%. This proportion has to be considered as the maximum possible content of gibbsite in the system. On the other hand, if the excess is only due to missing silicon tetrahedra in the internal cavity, considering 16 structural units per imogolite circumference, then sample 1 would have 5 missing Si tetrahedra. Obviously, the measured ratio is most probably a combination of both lacunae and impurities.

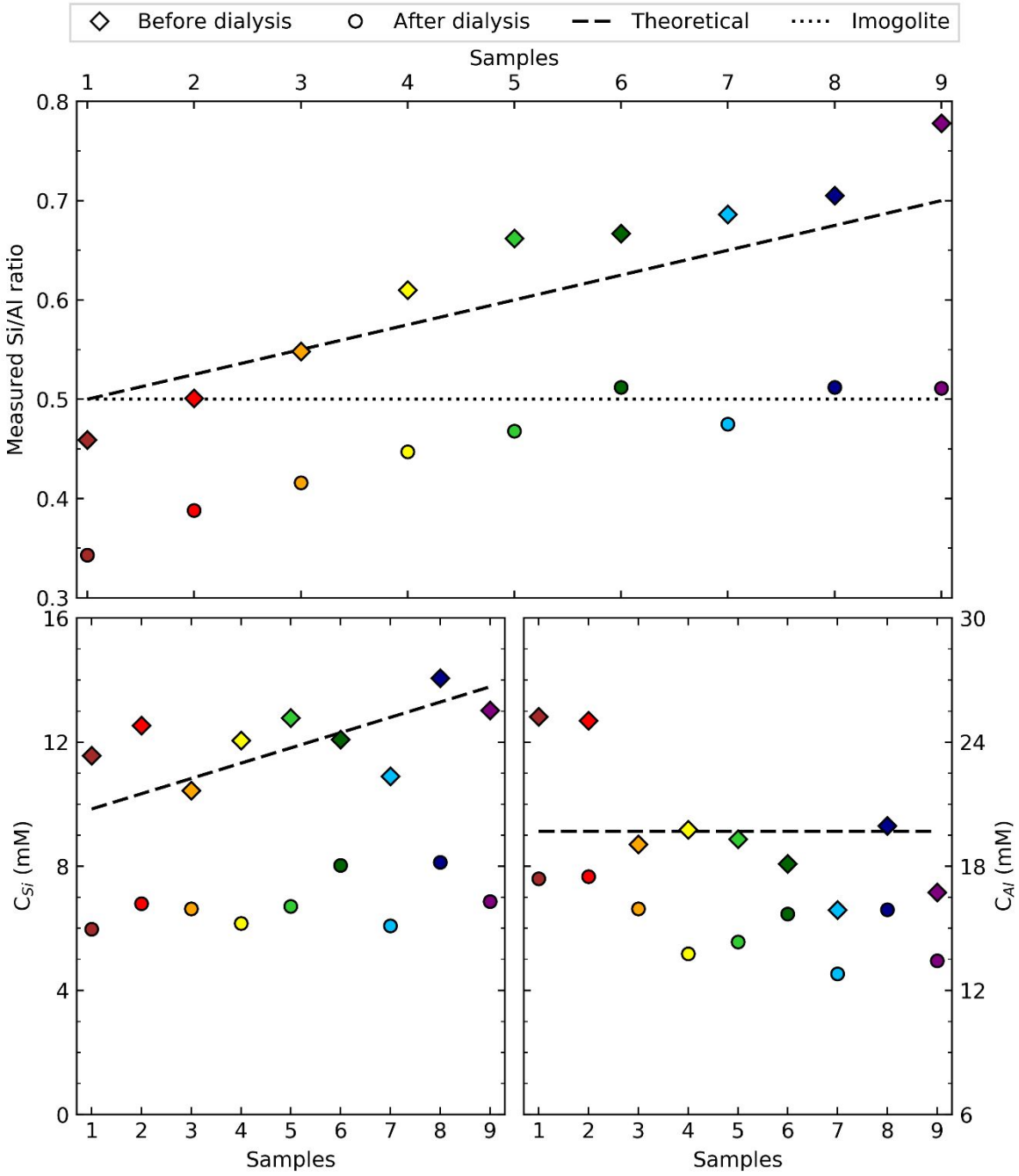

Figure 2 - Top chart: measured Si/Al ratio; bottom left and right charts are respectively the measured Si and Al concentrations. Diamonds correspond to measurement before dialysis, circles after dialysis, dashed line to theoretical values and finally dotted line correspond to stoichiometric ratio of imogolite.

Armchair open-ImoLS (2,2)

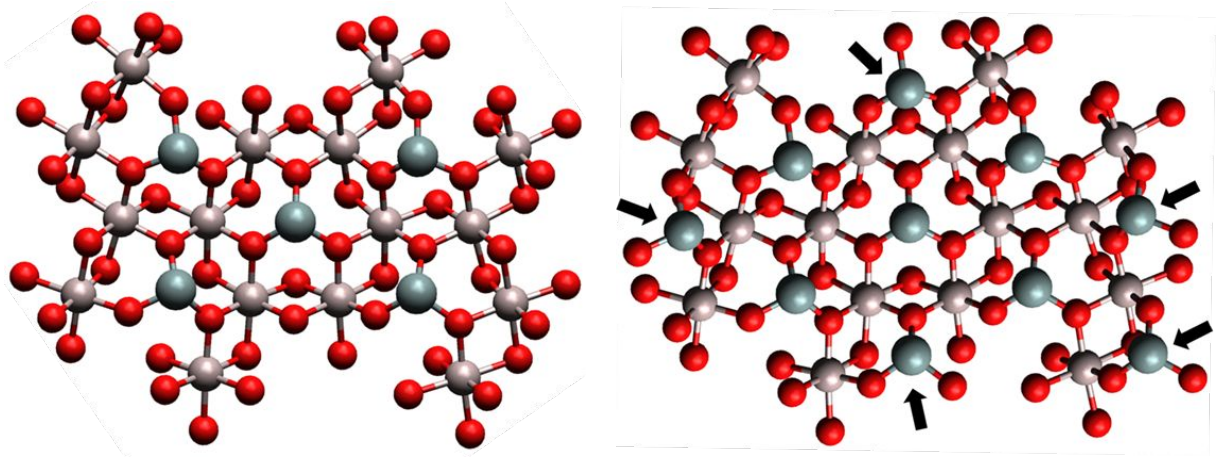

Si/Al = 0.313 Si/Al = 0.625

Armchair open-ImoLS (3,4)

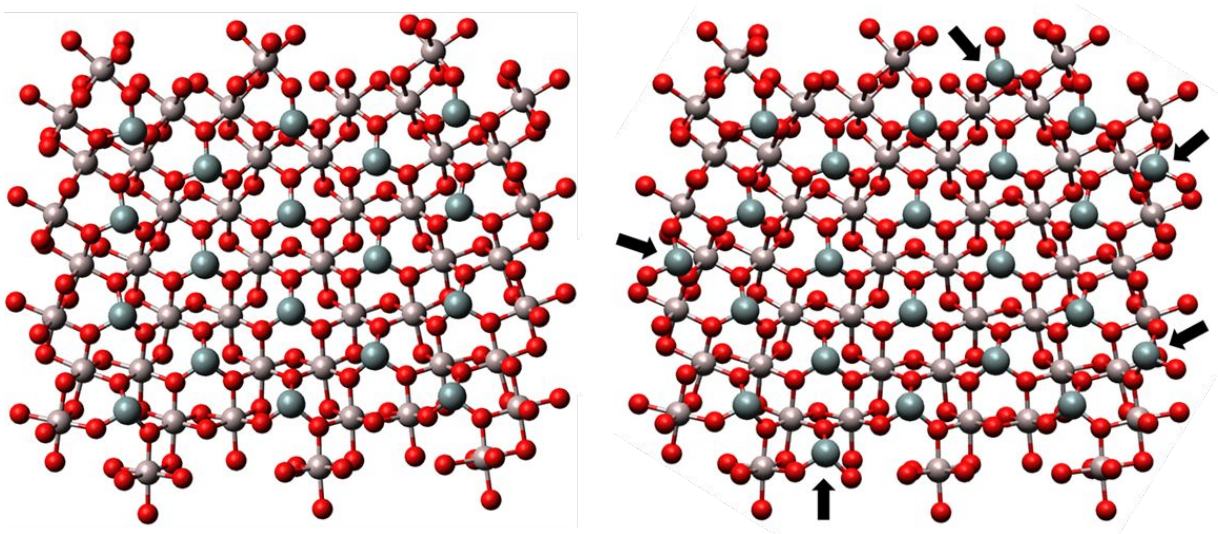

Si/Al = 0.375 Si/Al = 0.479

Scheme 1 – Armchair open-ImoLS configurations (2,2) (top) and (3,4) (bottom). Left side corresponds to pristine open-ImoLS and right side to totally (top) or partially (bottom) covered edges with Si tetrahedra. Red, brown and grey atoms are respectively oxygen, aluminum and silicon atoms. For the sake of clarity, carbons and hydrogens are omitted. Black arrows highlight added silicon tetrahedra.

Infrared

Figure 3 shows the IR spectra of the samples after dialysis. The doublet at 960/910 cm^{-1} (Si–O–Al stretching) and the adsorption bands at 680/575/545 cm^{-1} (Al–O modes), 510 cm^{-1} (O–Si–O bending) and 420 cm^{-1} (O–Al–O bending) are characteristic of the imogolite tubular structure.[21, 32, 34-36, 40] The peaks at 2976/2926 cm^{-1} (CH_3/CH_2 asymmetric stretching), 1273 cm^{-1} (CH_3 symmetric deformation in Si–CH_3) and 780 cm^{-1} (methyl rocking and Si–C) corroborate the presence of methyl groups.[32, 35, 36, 40, 42-45]

For all the dispersions, the typical peaks of imo-CH_3 are present. Nevertheless, for initial Si/Al ratio below 0.65, additional peaks are noticeable in the 4000 – 2800 cm^{-1} range. Some of them can be associated with the presence of gibbsite (γ–$Al(OH)_3$) and/or bayerite (α–$Al(OH)_3$). These two minerals are polymorphs that differ only by their packing. For α–$Al(OH)_3$ the packing order is ABAB (*i.e.* one interlayer distance) whereas for γ-$Al(OH)_3$ the order is AABBAABB (*i.e.* two interlayer distances).[46] Bands at 3563/3548 cm^{-1} are due to bayerite, those at 3390/3370 cm^{-1} to gibbsite while peaks at 3656/3621/3527/3480/3430 cm^{-1} can correspond to both bayerite and gibbsite.[47-51] The peaks at 1060/1020/760 cm^{-1} confirm the presence of these two phases.[47-50] The relative abundance of these two minerals and its evolution with initial Si/Al ratio is difficult to assess on the sole basis of FTIR results, especially considering that the shape (sphere, plate, needle…) of the clay particles may influence their infrared spectra.[52, 53] However, the analysis of the IR spectra enables us to confirm the impact of the Si/Al ratio on the formation of one of the side products, aluminum hydroxide, whose proportion decreases when the molar ratio increases.

Table 1 - Relative absorbance ratio measured between the peaks at 910 and 960 cm^{-1}.

Sample	Si/Al ratio measured by ICPMS		Measured ratio A_{910}/A_{960}
	Before dialysis	After dialysis	
1	0.459	0.343	1.029
2	0.501	0.388	1.046
3	0.548	0.416	1.059
4	0.610	0.447	1.080
5	0.662	0.468	1.070
6	0.667	0.512	1.045
7	0.686	0.475	1.072
8	0.705	0.512	1.056
9	0.778	0.511	1.062

Concerning the other side product, *i.e.* spherical closed/open-ImoLS, the analysis of the IR spectra is more complex. The doublet assigned to Si–O–Al bond is characteristic of the tubular structure. Imogolite is formed thanks to the bonding of silicon tetrahedra to a $Al(OH)_3$ layer via three Si–O–Al bonds. In an imogolite tubular structure, the alignment of these bonds with respect to the tube axis is different between the three bonds. Therefore, the three Si–O–Al bonds are not equivalent, leading to a doublet at 910 and 960 cm^{-1}. In a spherical structural configuration, there is no longer any particular privileged

orientation and the three Si–O–Al bonds are identical. Therefore, for spherical closed/open-ImoLS, only one peak is observed at 945 cm^{-1}. Hence, the relative absorbance ratio between the 910 and 960 cm^{-1} peaks is sensitive to the proportion of tubular versus spherical ImoLS.[38] Unfortunately, this spectral range (~1000 cm^{-1}) is also strongly affected by the presence of aluminum hydroxide and by the mechanical treatment of the powder.[54] This is illustrated by the fact that the intensity of the peaks are completely modified between imogolite measured with KBr pellet or self-supported films.[36] Nevertheless, it is possible to qualitatively assess measured evolutions in our experiments (Table 1). Here again, two regimes can be identified: for samples 1 to 4, the A_{910}/A_{960} intensity ratio increases with Si content up to a maximum for an initial Si/Al ratio of 0.6, probably due to the reduction of aluminum hydroxide amount. For higher Si content (sample 5 to 9), the A_{910}/A_{960} intensity ratio is systematically smaller, probably reflecting a higher proportion of spherical closed/open-ImoLS compounds in the dispersion as suggested by cryo-TEM images

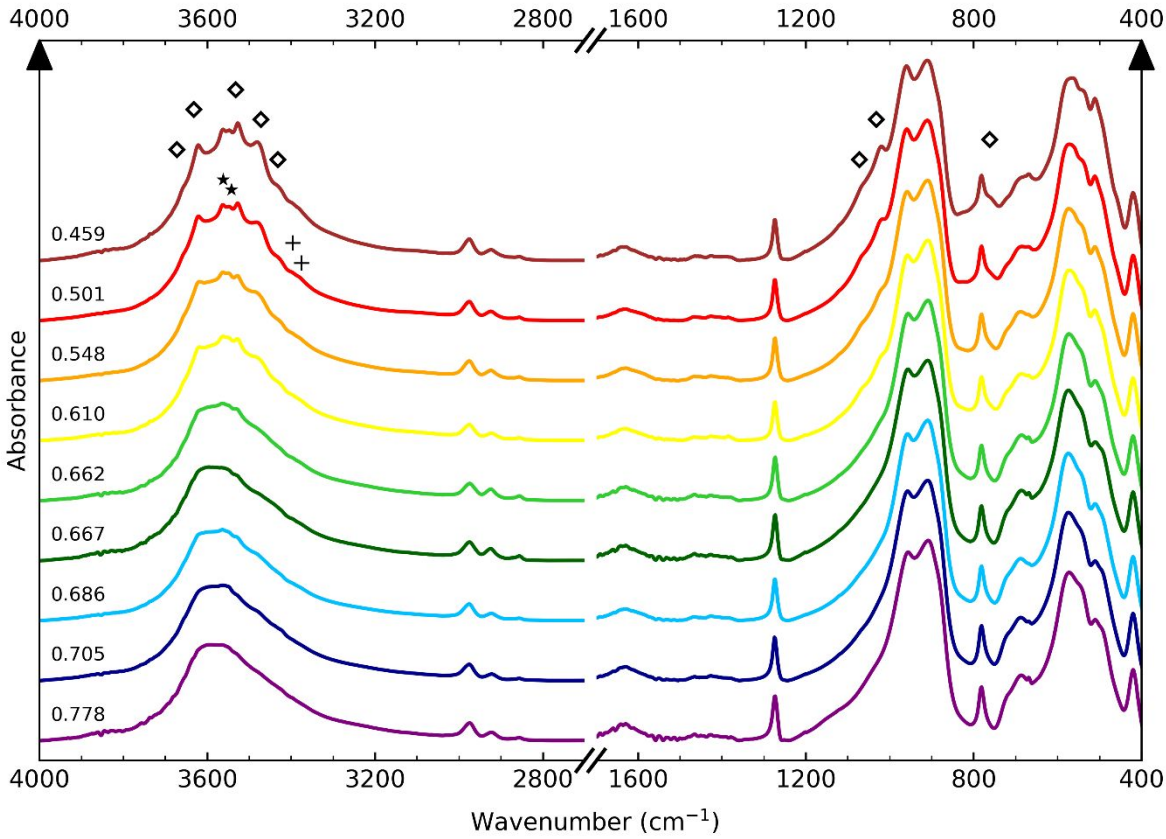

Figure 3 - IR spectra of the nine samples. Si/Al ratios before dialysis are written above corresponding curves. Stars, cross and diamonds corresponds to bayerite, gibbsite and both aluminum hydroxides, respectively. For the sake of clarity, the curves have been translated.

SAXS

Figure 4 displays the SAXS curves of the samples before (dashed lines) and after (solid lines) dialysis. The most striking effect of the dialysis step is the shift of the position of the first minimum $q_{I_{min_1}}$. SAXS data are very sensitive to internal electronic density (IED), *i.e.* what is inside the nanotube, which strongly influences the position of $q_{I_{min_1}}$. For instance for classical imogolite, with hydroxyl groups, IED is 0.334 $e^{-}\cdot Å^{-3}$ corresponding to the value of bulk water. For methyl-imogolite, IED is lower than the value of bulk water, between 0.17 and 0.11 $e^{-}\cdot Å^{-3}$.[32, 34, 35] The oscillations of the scattering curves are also very sensitive to the radius and thickness of the imogolite wall. Here, a deformation of the first maximum peak is observed at about 0.35 $Å^{-1}$, which can be attributed to the bundling of the nanotubes. To take into account this bundling, we assume the nanotubes to form small pieces of 2D hexagonal packing.[34] It should be noted that the shoulders or the holes around 0.4 $Å^{-1}$ observed for some curves are due to bad subtraction of Kapton capillary and water, slight variation of Kapton thickness (Figures S6 and S7).

In order to determine the structural parameters of the synthesized nanotubes from the experimental scattering curves, we have adjusted a core-shell cylinder model to our data. Parameters used are depicted in Table 2. Model parameters are consistent with previous observations.[16, 30, 32, 34, 35, 55]

*Table 2 - Parameters used in the core-shell cylinder model in this study and previous ones. *Aluminum octahedra, in imogolite, exhibit the same hexagonal arrangement that carbon in a graphene sheet. Consequently, the formalism used to describe carbon nanotubes is applied. The nanotubes are noted (n,m) where n and m are the components of the chiral vector in the hexagonal basis.[41, 55]*

Parameters	This study	[30]	[32]	[34]	[35]	[55]
Internal radius (Å)	9	9.85	9	9.1	9	9
Wall thickness (Å)	6	5	7	6	6	5.3
Indexes of the chiral vector*	(16,0)	–	–	(13,0)	(15,0)	(9,9)
Period (Å)	8.6	–	–	8.5	8.5	4.89
Length (Å)	2000	–	–	200	3000	–
External electronic density ($e^{-}\cdot Å^{-3}$)	0.334	–	–	–	–	–

Figure 5 displays the values of IED obtained for the samples before (diamonds) and after (circles) dialysis using a mono hollow cylinder model with parameters described in Table 2. A substantial decrease of IED results from the dialysis step, from 0.25 – 0.12 $e^{-}\cdot Å^{-3}$ to 0.10 – 0.03 $e^{-}\cdot Å^{-3}$. Throughout the synthesis, methanol and butan-2-ol are produced during the hydrolysis of the precursors. These molecules have a strong affinity for the internal cavity.[34] We can therefore interpret the decrease of the IED during dialysis by an elimination of a significant proportion of the trapped alcohols. However, if only water is present at the end of dialysis, IED would correspond to more water than determined by Liao et *al.*[56] Indeed, in their study, imogolites have been dried at high temperature and under vacuum. This process eliminates trapped molecules more efficiently than dialysis. Furthermore, IED decreases when the Si/Al ratio increases. This can be attributed to the reduction of defects in the internal Si layer. If some tetrahedra are missing, then Al–OH groups will be pointing inside the cavity. At these defects, water molecules could be trapped leading to a higher IED.

Importantly, the position of $q_{I_{min_1}}$ is also affected by the proportion of aluminum hydroxide, spherical open-ImoLS and closed-ImoLS (allophane) in the dispersion. Consequently, IED is a parameter of the model and it is adjusted to fit the position of $q_{I_{min_1}}$. In order to quantify the proportion of the different species, SAXS curves are fitted combining models from each species. Imogolite and aluminum platelets are assumed to be represented by analytical scattering models for slightly agglomerated cylinders and a homogenous cylinder platelet, respectively.[57, 58] The model used for methyl-imogolite takes into account the presence of bundles of 1, 2, 3 and 4 nanotubes. As described by Amara et *al.*, the first oscillation of imo–CH_3 SAXS curve is deformed (compare to imo–OH) by a correlation peak around 0.35 $Å^{-1}$ due to the formation of these bundles.[34]

For cylinder platelets, we use the Porod's law:

$$\lim_{q\to\infty} q^4 I(q) = 2\pi(\rho_{AH} - \rho_W)\frac{S_{AH}}{V} = 4\pi^2(\rho_{AH} - \rho_W)\frac{(r^2 + re)}{V}$$

With $\rho_{AH} = 2.04 \times 10^{11}\ cm^{-2}$ and $\rho_w = 9.43 \times 10^{10}\ cm^{-2}$ the scattering length density of aluminium hydroxides and water, r and e are respectively the radius and the thickness of the cylinder and $V = 1\ cm^3$ the volume in which we consider the particle. A value of $r = 82\ nm$ is obtained by averaging the surface of aluminum hydroxides from cryo-TEM images and assuming a disk of same surface (instead of a hexagonal shape). Aluminum hydroxides platelets tend to pack, forming aggregates of few tens sheets. We consider here a thickness of 25 nm in agreement with previous papers regarding the ratio between r and e.[59, 60]

For spherical closed-ImoLS (allophane) and open-ImoLS, scattering is computed from structural models using the Debye formula. The open-ImoLS models (scheme 1) are constructed and relaxed as previously explained with configuration ranging from (1,2) to (5,10).[41] For allophane, we have adopted the model proposed by Creton.[61] This allophane model is also relaxed using simple harmonic bonds for Si–O and Al–O stretching and O–Si–O and O–Al–O bending using the same constants as for open-ImoLS. The relaxations are performed with the LAMMPS software. Trajectories of 120 ps are calculated and an average structure obtained from the second half of the trajectory is considered for the scattering calculation. The calculated scattering does not take into account the solvent. Assuming a homogeneous solvent of average scattering length density ρ_w, we have rescaled the obtained form factor by $(\rho_{imo} - \rho_w)^2/{\rho_{imo}}^2$ with $\rho_{imo} = 2.32 \times 10^{11}\ cm^{-2}$ the scattering length density of methyl-imogolite.

In addition, the number of Si atoms that can be linked to the edges of open-ImoLS compounds is a fitting parameter, which can be varied between no tetrahedron to fully covered edges. Here, only tetrahedra bonded with two Si–O–Al to the aluminum octahedral respecting the ImoLS are considered (scheme 1).

Finally, in order to take into account the ratios measured by ICPMS, constraints on Al and Si concentrations are applied during the fitting procedure. For each sample, the concentrations of silicon and aluminum are calculated and an error of less than 10% is allowed between the measured and the fitted concentrations for the two atoms. Finally, due to poor subtractions of Kapton and water, only the *q* range between 3.68×10^{-2} to 3.5×10^{-1} $Å^{-1}$ and 4.9×10^{-1} to 7.0×10^{-1} $Å^{-1}$ is used for the fit.

The fitting procedure relies on several hypotheses. For instance, aluminum hydroxides are represented by homogenous cylinder platelets with the same radius for the nine samples. In addition, only open-ImoLS can exhibit Si/Al above 0.5 whereas imogolites should also have a Si/Al ratio slightly above 0.5. Therefore, the results should not be considered strictly quantitative.

Figure 6 displays the SAXS curves of samples 3 and 8 with Si/Al ratio after dialysis of 0.416 (top chart) and 0.512 (bottom chart) and the resulting fit with the different components. The others comparisons between experimental and model data are displayed in Figure S8a-i. The fit correctly reproduce the position and intensity of the first minimum that is very sensitive to the ratio of the different compounds. The fit is not perfect at higher q values. The model displays oscillations around q = 0.6 $Å^{-1}$ that are not observed experimentally. These oscillations are due to the packing model for the nanotubes and to the presence of allophane. Cryo-TEM pictures clearly indicate that the bundling is limited to 2 to 4 nanotubes in a geometry that is more complex than the assumed perfect 2D hexagonal packing (see Figure S2). The packing used in the model overestimates the oscillation amplitude. Moreover, the defect-free model of allophane also contributes to this overestimation of the high q oscillations. The model is based on many hypothesis and depends on many parameters, and so, by itself, it would not be trustworthy. However, its coupling with the techniques reported previously (cryo-TEM, ICPMS and IR) enables to confirm some tendencies consistently. Figure 7 displays the mass repartition of the different species obtained by the fit of the nine samples and weight percentage of aluminum hydroxide obtained with ICPMS measurements. It should be noted that the proportion of aluminum hydroxides decreases when the ratio Si/Al increases. Moreover, for this side product, the percentage obtained with SAXS fits and ICPMS measurements are consistent. The mass proportion of spherical closed-ImoLS (allophane) and open-ImoLS is increasing from 27 to 45%. The increase of the allophane content could mean that the initial ratio of Si precursor is not an effective way to significantly modify the average size of open-ImoLS structures. A constant proportion of open-ImoLS up to Si/Al ratio of 0.5 is observed. Above this, its proportion increases significantly. According to this observation, an optimal initial Si/Al ratio would be the minimum ratio, which enables to have a Si/Al ratio close to 0.5 after dialysis. In this particular case, it means an initial ratio around 0.65. Yet, at such optimal ratio, the side products still represent about 30 w%, even after dialysis. It is interesting to note that salt based protocol seems to give less proto-imogolite (< 5 w%) but the nanotubes are shorter (20 nm).[34]

Most of the fits previously performed on imogolite and especially on methyl-imogolite did not take into account the presence of side products even though they can represent half of the sample. This could lead to some mistakes if the quality of the dispersion is not tested. For instance, isoelectric point (IEP), pH where there are no surface charges, is not the same between imogolite and allophane. For the nanotube IEP is similar to the one of aluminum hydroxide, around 10,[62] whereas for allophane it is below 6.[63-65] Even if these values correspond to classical allophane and imogolite, with internal hydroxyl groups, we could easily assume the values of methyl ones should be similar to OH compounds. Consequently, depending on the proportions of the species in the final dispersion, IEP could vary from acid to alkaline condition.

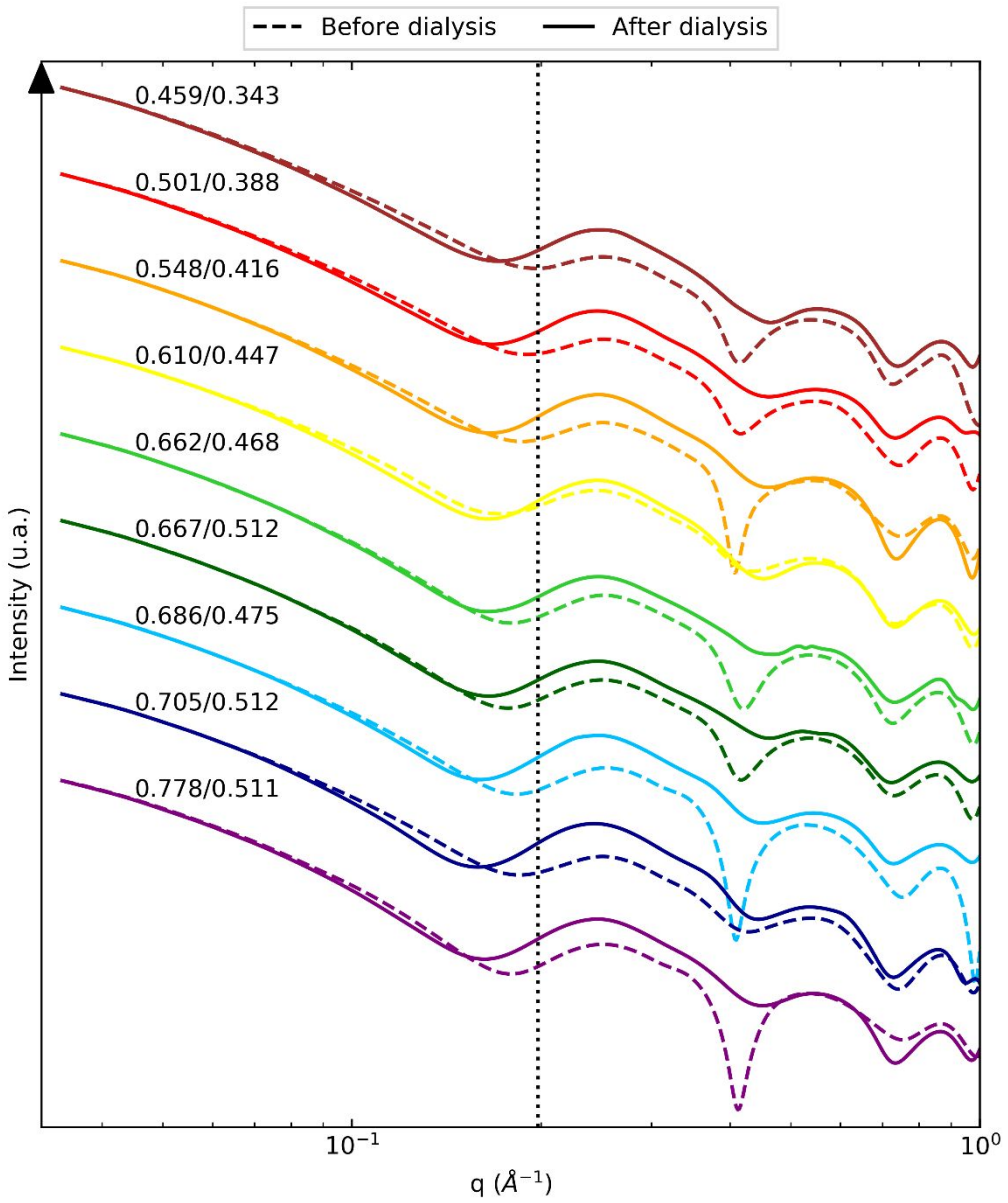

Figure 4 – SAXS curves of the samples before (dashed lines) and after (solid lines) dialysis. Si/Al ratio before and after dialysis are written above corresponding curves. For the sake of clarity, the curves have been translated.

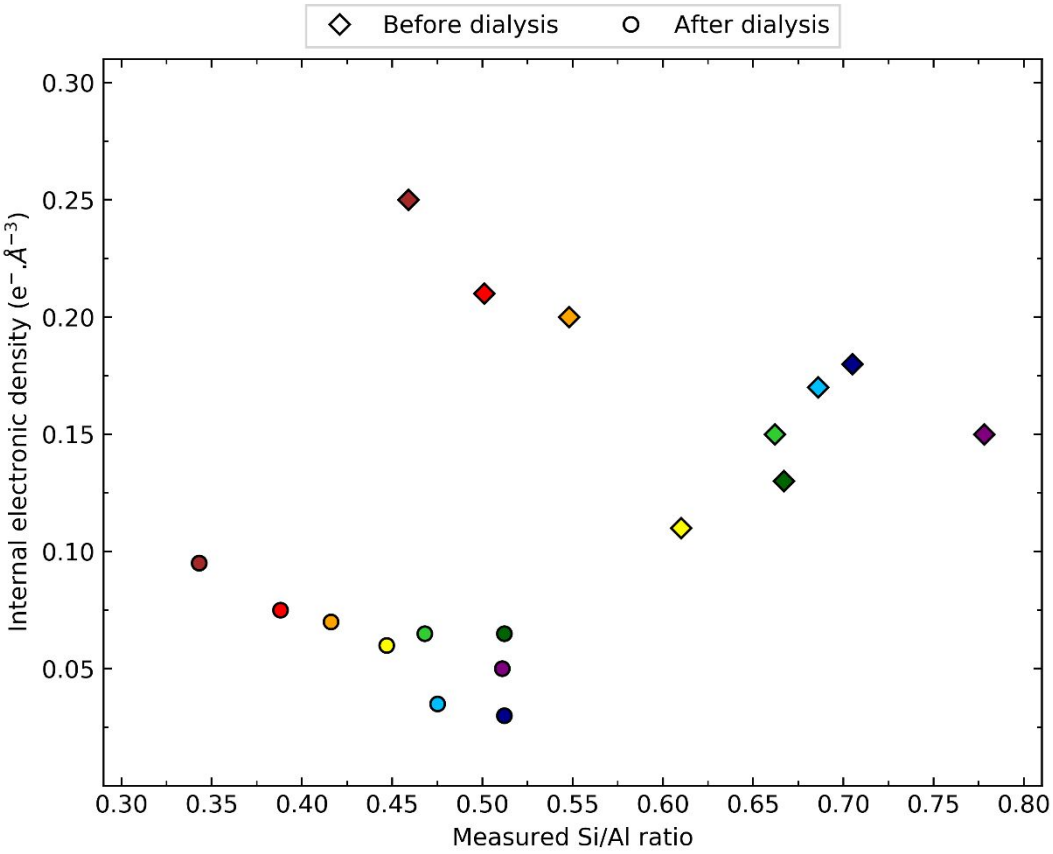

Figure 5 – Internal electronic density of the samples before (diamonds) and after (circles) dialysis.

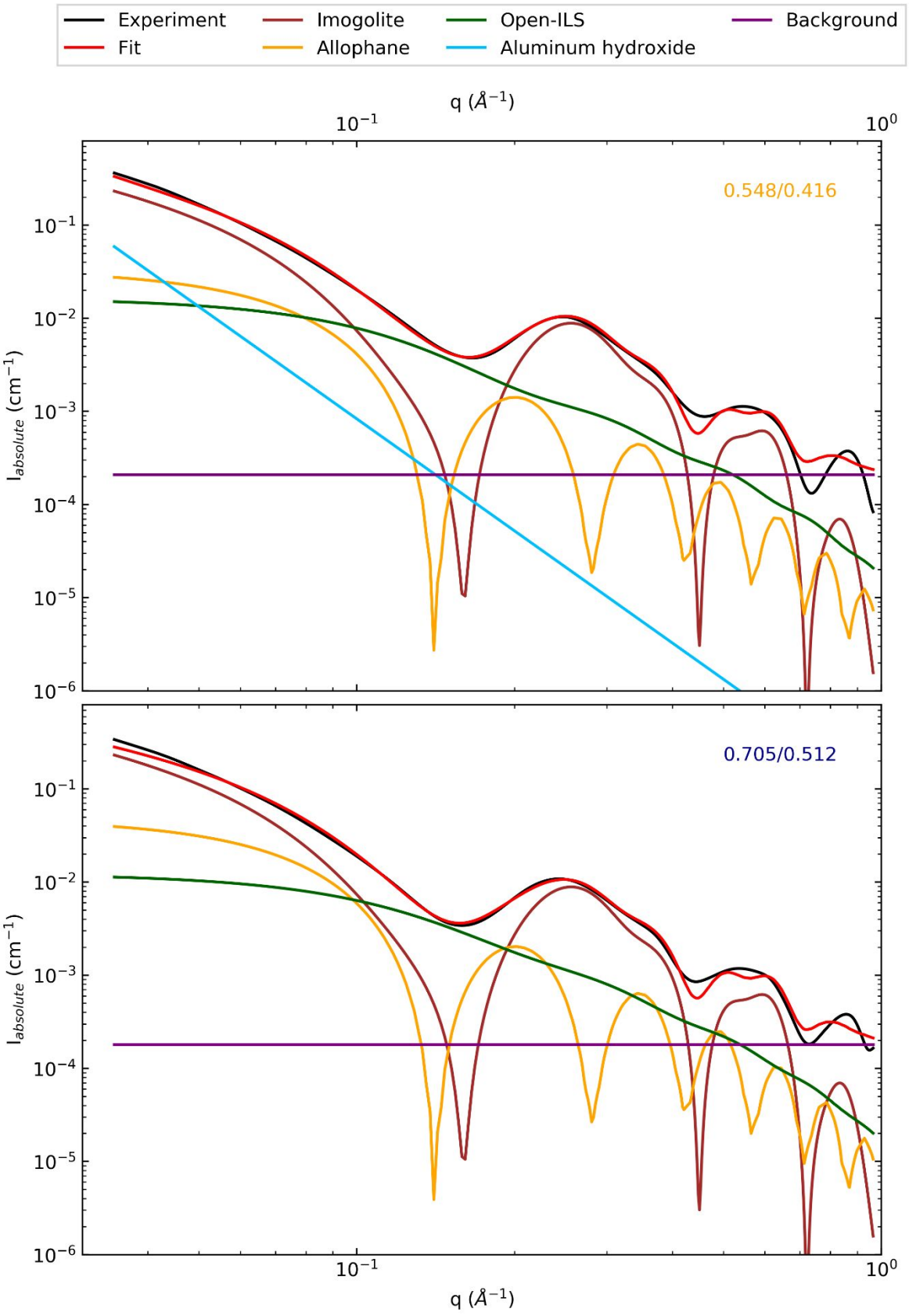
Experiment
Fit
Imogolite
Allophane
Open-ILS
Aluminum hydroxide
Background
q (Å^{-1})
10^{-1}
10^{0}
0.548/0.416
0.705/0.512
$I_{absolute}$ (cm^{-1})
10^{-1}
10^{-2}
10^{-3}
10^{-4}
10^{-5}
10^{-6}

Figure 6 – SAXS curves of the dialyzed sample (black) and the resulting fit (red) of the different species: imogolite (brown), allophane (orange), open-ImoLS (dark green), aluminum hydroxide (blue) and background (purple). Top chart corresponds to sample 3 with ratio Si/Al before and after dialysis of 0.548 and 0.416; bottom chart corresponds to sample 8 with ratio Si/Al before and after dialysis of 0.705 and 0.512.

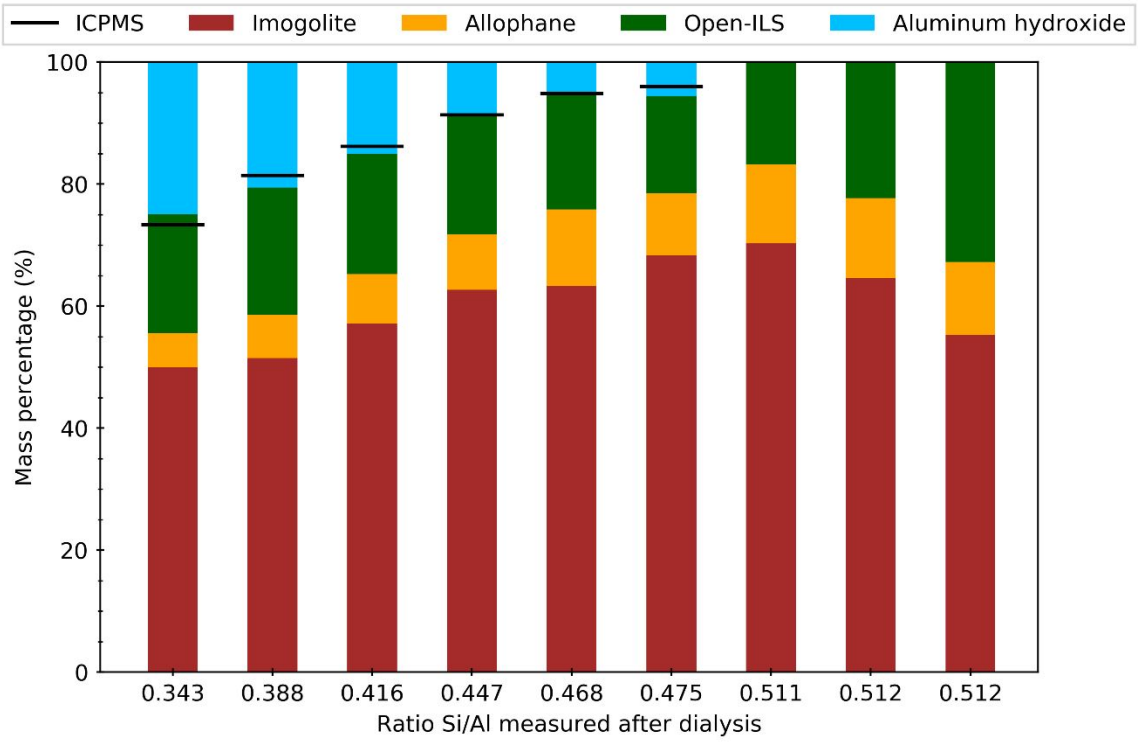

Figure 7 - Mass distribution of the different species for the nine samples: imogolite (brown), allophane (orange), open-ImoLS (dark green) and aluminum hydroxide (blue). Black lines correspond to the maximum aluminum hydroxide weight percentage obtained by ICPMS measurements.

Conclusion

While the presence of side products in synthetic imogolite dispersions has been known for a long time, our results enlighten that their nature and relative abundance is strongly dictated by initial Si/Al ratio. In the low Si/Al regime, aluminum hydroxides are the main additional phases while spherical closed/open-ImoLS become more abundant in the high Si/Al regime. Whereas it is not possible to avoid their formation by simply varying this ratio, our different analysis show that there is an optimal initial Si/Al ratio between 0.6 and 0.65 which enables to minimize both side products. Additional post-treatments may allow for further purification. For example, centrifugation is very efficient to remove aluminum hydroxides while ultrafiltration with large cut-off membrane may allow for the separation of open-ImoLS. However, if these side products are the result of a thermodynamic equilibrium, their removal may result in the dissolution of imogolite and formation of new ones. While this point will have to be clarified in a near future, our results already suggest that dispersed imogolite nanotubes should not be considered as inert structures but rather as dynamic reactive nanomaterials.

Supporting Information

Pictures of samples 1 and 9; Cryo-TEM images of samples 1, 5 and 2; evolution of Si/Al ratio for open-ImoLS of increasing size; evolution of crossed thickness by a beam and SAXS curves associated; SAXS diagrams of water subtracted from Kapton capillary; SAXS curves of samples 1 to 9 with their fit.

Authors information

Corresponding Author
*E-mail: antoine.thill@cea.fr

Notes
The authors declare no competing financial interest.

Acknowledgments

This research is supported by public grant overseen by the French National Research Agency (ANR) as part of the “Investissements d’Avenir” program (Labex NanoSaclay, reference: ANR-10-LABX-0035). P.P. thanks the Région Ile-de-France for PhD funding (HIPPOP grant) in the framework of C'Nano IdF. C'Nano-IdF is the nanoscience competence center of Paris Region, supported by CNRS, CEA, MESR and Région Ile-de-France. We thank Barbara Bonelli for her precious advices concerning the recipe of methyl-imogolite. We are grateful for access to SOLEIL synchrotron and SWING line (proposal 20160545). We thank Dr Perez Javier and Dr Bizien Thomas for the preparation of the SAXS line. We also thank David Carrière and Alexy Freitas for their time and participation during the nights in SOLEIL synchrotron. Cryo-TEM observations

were made thanks to “Investissements d’Avenir” LabEx PALM (ANR-10-LABX-0039-PALM). We also thanks Jéril Degrouard for his time and its help. We graciously thank referee 1 who allowed us to improve greatly the manuscript.

References

1. Colombo, M.; Nova, I.; Tronconi, E., A comparative study of the NH3-SCR reactions over a Cu-zeolite and a Fe-zeolite catalyst. *Catalysis Today* **2010,** *151* (3-4), 223-230.
2. Liu, Y.; Pinnavaia, T. J., Aluminosilicate nanoparticles for catalytic hydrocarbon cracking. *Journal of the American Chemical Society* **2003,** *125* (9), 2376-2377.
3. Datt, A.; Fields, D.; Larsen, S. C., An Experimental and Computational Study of the Loading and Release of Aspirin from Zeolite HY. *Journal of Physical Chemistry C* **2012,** *116* (40), 21382-21390.
4. Jin, J.; Gao, H.; Chen, X.; Peng, Y.; Min, F., The flotation of aluminosilicate polymorphic minerals with anionic and cationic collectors. *Minerals Engineering* **2016,** *99*, 123-132.
5. Ogura, M.; Kawazu, Y.; Takahashi, H.; Okubo, T., Aluminosilicate species in the hydrogel phase formed during the aging process for the crystallization of FAU zeolite. *Chemistry of Materials* **2003,** *15* (13), 2661-2667.
6. Maldonado, M.; Oleksiak, M. D.; Chinta, S.; Rimer, J. D., Controlling Crystal Polymorphism in Organic-Free Synthesis of Na-Zeolites. *Journal of the American Chemical Society* **2013,** *135* (7), 2641-2652.
7. Yoshinaga, N.; Aomine, S., Imogolite In Some Ando Soils. *Soil Science and Plant Nutritution* **1962,** *8* (3), 22-29.
8. Gabriel, J. C. P.; Davidson, P., Mineral liquid crystals from self-assembly of anisotropic nanosystems. In *Colloid Chemistry 1*, Antonietti, M., Ed. 2003; Vol. 226, pp 119-172.
9. Tamura, K.; Kawamura, K., Molecular dynamics modeling of tubular aluminum silicate: Imogolite. *Journal of Physical Chemistry B* **2002,** *106* (2), 271-278.
10. Jiravanichanun, N.; Yamamoto, K.; Kato, K.; Kim, J.; Horiuchi, S.; Yah, W.-O.; Otsuka, H.; Takahara, A., Preparation and Characterization of Imogolite/DNA Hybrid Hydrogels. *Biomacromolecules* **2012,** *13* (1), 276-281.
11. Cradwick, P. D.; Wada, K.; Russell, J. D.; Yoshinaga, N.; Masson, C. R.; Farmer, V. C., Imogolite, a hydrated aluminum silicate of tubular structure. *Nature-Physical Science* **1972,** *240* (104), 187-189.
12. Abidin, Z.; Matsue, N.; Henmi, T., Differential formation of allophane and imogolite: experimental and molecular orbital study. *Journal of Computer-Aided Materials Design* **2007,** *14* (1), 5-18.
13. Konduri, S.; Mukherjee, S.; Nair, S., Strain energy minimum and vibrational properties of single-walled aluminosilicate nanotubes. *Physical Review B* **2006,** *74* (3).
14. Teobaldi, G.; Beglitis, N. S.; Fisher, A. J.; Zerbetto, F.; Hofer, A. A., Hydroxyl vacancies in single-walled aluminosilicate and aluminogermanate nanotubes. *Journal of Physics-Condensed Matter* **2009,** *21* (19).
15. Alvarez-Ramirez, F., Ab initio simulation of the structural and electronic properties of aluminosilicate and aluminogermanate natotubes with imogolite-like structure. *Physical Review B* **2007,** *76* (12).
16. Guimaraes, L.; Enyashin, A. N.; Frenzel, J.; Heine, T.; Duarte, H. A.; Seifert, G., Imogolite nanotubes: Stability, electronic, and mechanical properties. *Acs Nano* **2007,** *1* (4), 362-368.

17. Paineau, E.; Krapf, M.-E. M.; Amara, M.-S.; Matskova, N. V.; Dozov, I.; Rouziere, S.; Thill, A.; Launois, P.; Davidson, P., A liquid-crystalline hexagonal columnar phase in highly-dilute suspensions of imogolite nanotubes. *Nature Communications* **2016,** *7*.
18. Lee, S. U.; Choi, Y. C.; Youm, S. G.; Sohn, D., Origin of the Strain Energy Minimum in Imogolite Nanotubes. *Journal of Physical Chemistry C* **2011,** *115* (13), 5226-5231.
19. Farmer, V. C.; Fraser, A. R.; Tait, J. M., Synthesis of imogolite: A tubular aluminum silicate polymer. *Journal of the Chemical Society-Chemical Communications* **1977,** (13), 462-463.
20. Wada, S., Imogolite synthesis at 25°C. *Clays and Clay Minerals* **1987,** *35* (5), 379-384.
21. Wada, S.; Wada, K., Effects of substitution of germanium for silicon in imogolite. *Clays and Clay Minerals* **1982,** *30* (2), 123-128.
22. Avellan, A.; Levard, C.; Kumar, N.; Rose, J.; Olivi, L.; Thill, A.; Chaurand, P.; Borschneck, D.; Masion, A., Structural incorporation of iron into Ge-imogolite nanotubes: a promising step for innovative nanomaterials. *Rsc Advances* **2014,** *4* (91), 49827-49830.
23. Shafia, E.; Esposito, S.; Armandi, M.; Manzoli, M.; Garrone, E.; Bonelli, B., Isomorphic substitution of aluminium by iron into single-walled alumino-silicate nanotubes: A physico-chemical insight into the structural and adsorption properties of Fe-doped imogolite. *Microporous and Mesoporous Materials* **2016,** *224*, 229-238.
24. Yucelen, G. I.; Kang, D.-Y.; Guerrero-Ferreira, R. C.; Wright, E. R.; Beckham, H. W.; Nair, S., Shaping Single-Walled Metal Oxide Nanotubes from Precursors of Controlled Curvature. *Nano Letters* **2012,** *12* (2), 827-832.
25. Ma, W.; Otsuka, H.; Takahara, A., Poly(methyl methacrylate) grafted imogolite nanotubes prepared through surface-initiated ARGET ATRP. *Chemical Communications* **2011,** *47* (20), 5813-5815.
26. Yamamoto, K.; Otsuka, H.; Wada, S.; Takahara, A., Surface modification of aluminosilicate nanofiber "imogolite". *Chemistry Letters* **2001,** (11), 1162-1163.
27. Yamamoto, K.; Otsuka, H.; Wada, S. I.; Sohn, D.; Takahara, A., Preparation and properties of poly(methyl methacrylate)/imogolite hybrid via surface modification using phosphoric acid ester. *Polymer* **2005,** *46* (26), 12386-12392.
28. Park, S.; Lee, Y.; Kim, B.; Lee, J.; Jeong, Y.; Noh, J.; Takahara, A.; Sohn, D., Two-dimensional alignment of imogolite on a solid surface. *Chemical Communications* **2007,** (28), 2917-2919.
29. Kang, D.-Y.; Brunelli, N. A.; Yucelen, G. I.; Venkatasubramanian, A.; Zang, J.; Leisen, J.; Hesketh, P. J.; Jones, C. W.; Nair, S., Direct synthesis of single-walled aminoaluminosilicate nanotubes with enhanced molecular adsorption selectivity. *Nature Communications* **2014,** *5*.
30. Bottero, I.; Bonelli, B.; Ashbrook, S. E.; Wright, P. A.; Zhou, W.; Tagliabue, M.; Armandi, M.; Garrone, E., Synthesis and characterization of hybrid organic/inorganic nanotubes of the imogolite type and their behaviour towards methane adsorption. *Physical Chemistry Chemical Physics* **2011,** *13* (2), 744-750.
31. Poli, E.; Elliott, J. D.; Ratcliff, L. E.; Andrinopoulos, L.; Dziedzic, J.; Hine, N. D. M.; Mostofi, A. A.; Skylaris, C. K.; Haynes, P. D.; Teobaldi, G., The potential of imogolite nanotubes as (co-)photocatalysts: a linear-scaling density functional theory study. *Journal of Physics-Condensed Matter* **2016,** *28* (7), 17.
32. Boyer, M.; Paineau, E.; Bacia-Verloop, M.; Thill, A., Aqueous dispersion state of amphiphilic hybrid aluminosilicate nanotubes. *Applied Clay Science* **2014,** *96*, 45-49.
33. Elliott, J. D.; Poli, E.; Scivetti, I.; Ratcliff, L. E.; Andrinopoulos, L.; Dziedzic, J.; Hine, N. D. M.; Mostofi, A. A.; Skylaris, C.-K.; Haynes, P. D.; Teobaldi, G., Chemically Selective Alternatives to Photoferroelectrics for Polarization-Enhanced Photocatalysis: The Untapped Potential of Hybrid Inorganic Nanotubes. *Advanced Science* **2017,** *4* (2).
34. Amara, M. S.; Paineau, E.; Rouziere, S.; Guiose, B.; Krapf, M. E. M.; Tache, O.; Launois, P.; Thill, A., Hybrid, Tunable-Diameter, Metal Oxide Nanotubes for Trapping of Organic Molecules. *Chemistry of Materials* **2015,** *27* (5), 1488-1494.

35. Picot, P.; Tache, O.; Malloggi, F.; Coradin, T.; Thill, A., Behaviour of hybrid inside/out Janus nanotubes at an oil/water interface. A route to self-assembled nanofluidics? *Faraday Discussions* **2016,** *191*, 391-406.
36. Liao, Y.; Picot, P.; Brubach, J.-B.; Roy, P.; Le Caër, S.; Thill, A., Self-supporting thin films of imogolite and imogolite-like nanotubes for infrared spectroscopy. *Applied Clay Science* **2017**.
37. Levard, C.; Doelsch, E.; Basile-Doelsch, I.; Abidin, Z.; Miche, H.; Masion, A.; Rose, J.; Borschneck, D.; Bottero, J. Y., Structure and distribution of allophanes, imogolite and proto-imogolite in volcanic soils. *Geoderma* **2012,** *183*, 100-108.
38. Du, P.; Yuan, P.; Thill, A.; Annabi-Bergaya, F.; Liu, D.; Wang, S., Insights into the formation mechanism of imogolite from a full-range observation of its sol-gel growth. *Applied Clay Science* **2017,** *150*, 115-124.
39. Maillet, P.; Levard, C.; Spalla, O.; Masion, A.; Rose, J.; Thill, A., Growth kinetic of single and double-walled aluminogermanate imogolite-like nanotubes: an experimental and modeling approach. *Physical Chemistry Chemical Physics* **2011,** *13* (7), 2682-2689.
40. Zanzottera, C. Hybrid organic/inorganic nanotubes of imogolite type. Politecnico di Torino, 2011.
41. Thill, A.; Picot, P.; Belloni, L., A mechanism for the sphere/tube shape transition of nanoparticles with an imogolite local structure (imogolite and allophane). *Applied Clay Science* **2017,** *141*, 308-315.
42. Mendelovici, E.; Portillo, D. C., Organic derivatives of attapulgite - I. Infrared spectroscopy and X-ray diffraction studies. *Clays and Clay Minerals* **1976,** *24* (4), 177-182.
43. Shimomura, M.; Kyotani, H.; Kaito, A., Methyl rocking vibrational modes of poly(dimethylsilane). *Macromolecules* **1997,** *30* (24), 7604-7606.
44. Frost, R. L.; Mendelovici, E., Modification of fibrous silicates surfaces with organic derivatives: An infrared spectroscopic study. *Journal of Colloid and Interface Science* **2006,** *294* (1), 47-52.
45. Al-Oweini, R.; El-Rassy, H., Synthesis and characterization by FTIR spectroscopy of silica aerogels prepared using several Si(OR)(4) and R '' Si(OR ')(3) precursors. *Journal of Molecular Structure* **2009,** *919* (1-3), 140-145.
46. Demichelis, R.; Civalleri, B.; Noel, Y.; Meyer, A.; Dovesi, R., Structure and stability of aluminium trihydroxides bayerite and gibbsite: A quantum mechanical ab initio study with the CRYSTAL06 code. *Chemical Physics Letters* **2008,** *465* (4-6), 220-225.
47. Elderfield, H.; Hem, J. D., The development of crystalline-structure in aluminum hydroxide polymorphs on ageing. *Mineralogical Magazine* **1973,** *39* (301), 89-96.
48. Chao, G. Y.; Baker, J.; Sabina, A. P.; Roberts, A. C., Doyleite, a new polymorph of Al(OH)3 and its relationship to bayerite, gibbsite and nordstrandite. *Canadian Mineralogist* **1985,** *23* (FEB), 21-28.
49. Fernandez-Carrasco, L.; Vazquez, T., Aplicación de la espectroscopia infrarroja al estudio de cemento aluminoso *Materiales de Construccion* **1996,** *46* (241), 53-65.
50. Kloprogge, J. T.; Ruan, H. D.; Frost, R. L., Thermal decomposition of bauxite minerals: infrared emission spectroscopy of gibbsite, boehmite and diaspore. *Journal of Materials Science* **2002,** *37* (6), 1121-1129.
51. Balan, E.; Refson, K.; Blanchard, M.; Delattre, S.; Lazzeri, M.; Ingrin, J.; Mauri, F.; Wright, K.; Winkler, B., Theoretical infrared absorption coefficient of OH groups in minerals. *American Mineralogist* **2008,** *93* (5-6), 950-953.
52. Balan, E.; Lazzeri, M.; Morin, G.; Mauri, F., First-principles study of the OH-stretching modes of gibbsite. *American Mineralogist* **2006,** *91* (1), 115-119.
53. Balan, E.; Blanchard, M.; Hochepied, J.-F.; Lazzeri, M., Surface modes in the infrared spectrum of hydrous minerals: the OH stretching modes of bayerite. *Physics and Chemistry of Minerals* **2008,** *35* (5), 279-285.
54. Henmi, T.; Yoshinaga, N., Alteration of imogolite by dry grinding. *Clay Minerals* **1981,** *16* (2), 139-149.

55. Monet, G.; Amara, M. S.; Rouziere, S.; Paineau, E.; Chai, Z.; Elliott, J. D.; Poli, E.; Liu, L.-M.; Teobaldi, G.; Launois, P., Structural resolution of inorganic nanotubes with complex stoichiometry. *Nature Communications* **2018,** *9*.
56. Liao, Y.; Picot, P.; Lainé, M.; Brubach, J.-B.; Roy, P.; Thill, A.; Le Caër, S., Tuning the properties of confined water in standard and hybrid nanotubes: An infrared spectroscopic study. *Nano Research* **2018,** *11* (9), 4759-4773.
57. Amara, M. S. Nanotubes d'imogolite et propriétés de l'eau confinée : organisation, structure et dynamique. Université Paris-Sud, 2014.
58. Pedersen, J. S., *Neutrons, X-rays and Light: Scattering Methods Applied to Soft Condensed Matter*. 1st edition ed.; Elsevier Science B.V.: Amsterdam, 2002; p 552.
59. Kleshchanok, D.; Heinen, M.; Naegele, G.; Holmqvist, P., Dynamics of charged gibbsite platelets in the isotropic phase. *Soft Matter* **2012,** *8* (5), 1584-1592.
60. Siretanu, I.; Ebeling, D.; Andersson, M. P.; Stipp, S. L. S.; Philipse, A.; Stuart, M. C.; van den Ende, D.; Mugele, F., Direct observation of ionic structure at solid-liquid interfaces: a deep look into the Stern Layer. *Scientific Reports* **2014,** *4*.
61. Creton, B. Etude par dynamique moléculaire du comportement d'aluminosilicates tubulaires hydratés : structure et dynamique du système eau-imogolite. Université des Sciences et Technologie de Lille, Lille, 2006.
62. Su, C. M.; Harsh, J. B., The electrophoretic mobility of imogolite and allophane in the presence of inorganic anions and citrate. *Clays and Clay Minerals* **1993,** *41* (4), 461-471.
63. Aomine, S.; Egashira, K., Flocculation of Allophanic clays by electrolytes. *Soil Science and Plant Nutrition* **1968,** *14* (3), 94-98.
64. Horikawa, Y., Electrokinetic phenomena of aqueous suspensions of allophane and imogolite. *Clay Science* **1975,** *4* (6), 255-263.
65. Taylor, D. H.; Bellamy, A. R.; Wilson, A. T., Interaction of bacteriophage R-17 and reovirus type-III with the clay mineral allophane. *Water Research* **1980,** *14* (4), 339-346.